ADVANCED ENERGY MATERIALS
www.advenergymat.de

Effect of Particle Size and Pressure on the Transport Properties of the Fast Ion Conductor *t*-Li_7SiPS_8

*Christian Schneider, Christoph P. Schmidt, Anton Neumann, Moritz Clausnitzer, Marcel Sadowski, Sascha Harm, Christoph Meier, Timo Danner, Karsten Albe, Arnulf Latz, Wolfgang A. Wall, and Bettina V. Lotsch**

All-solid-state batteries promise higher energy and power densities as well as increased safety compared to lithium-ion batteries by using non-flammable solid electrolytes and metallic lithium as the anode. Ensuring permanent and close contact between the components and individual particles is crucial for long-term operation of a solid-state cell. This study investigates the particle size dependent compression mechanics and ionic conductivity of the mechanically soft thiophosphate solid electrolyte tetragonal Li_7SiPS_8 (*t*-LiSiPS) under pressure. The effect of stack and pelletizing pressure is demonstrated as a powerful tool to influence the microstructure and, hence, ionic conductivity of *t*-LiSiPS. Heckel analysis for granular powder compression reveals distinct pressure regimes, which differently impact the Li ion conductivity. The pelletizing process is simulated using the discrete element method followed by finite volume analysis to disentangle the effects of pressure-dependent microstructure evolution from atomistic activation volume effects. Furthermore, it is found that the relative density of a tablet is a weaker descriptor for the sample's impedance compared to the particle size distribution. The multiscale experimental and theoretical study thus captures both atomistic and microstructural effects of pressure on the ionic conductivity, thus emphasizing the importance of microstructure, particle size distribution and pressure control in solid electrolytes.

1. Introduction

The global market for lithium-ion batteries (LIB) is expected to grow rapidly due to the need for high-energy storage media for consumer electronics and automotive applications. For battery electric vehicles (BEVs), high capacity is critical to compete with the high mileage of conventional internal combustion engine vehicles. The all-solid-state (lithium-ion) battery (ASSB), which is based on a solid rather than liquid electrolyte, promises to meet the growing energy needs of modern BEVs. The ASSB design not only enables bipolar stacking, but could also enable the use of high-capacity lithium metal- or silicon-based anodes as an alternative to low-capacity carbon-based anodes in LIBs.[1] These advantages in cell design promise to increase energy density by about 70% compared to conventional LIBs.[2] In a fully solid system, close contact between particles is required to generate homogeneous electric fields and minimize internal resistance. In industry, the consolidation of powdered starting materials

C. Schneider, S. Harm, B. V. Lotsch
Max Planck Institute for Solid State Research
Heisenbergstraße 1, 70569 Stuttgart, Germany
E-mail: b.lotsch@fkf.mpg.de

C. P. Schmidt, C. Meier, W. A. Wall
Technical University of Munich
Institute for Computational Mechanics
Bolzmannstraße 15, 85748 Garching bei München, Germany

A. Neumann, M. Clausnitzer, T. Danner, A. Latz
German Aerospace Center (DLR)
Institute of Engineering Thermodynamics
Pfaffenwaldring 38-40, 70569 Stuttgart, Germany

The ORCID identification number(s) for the author(s) of this article can be found under https://doi.org/10.1002/aenm.202203873.

DOI: 10.1002/aenm.202203873

A. Neumann, M. Clausnitzer, T. Danner, A. Latz
Helmholtz Institute Ulm for Electrochemical Energy Storage (HIU)
Helmholtzstraße 11, 89081 Ulm, Germany

M. Sadowski, K. Albe
Institute of Materials Science
Technical University of Darmstadt
Otto-Berndt-Straße 3, 64287 Darmstadt, Germany

S. Harm, B. V. Lotsch
Department of Chemistry, University of Munich (LMU)
Butenandstraße 5-13, 81377 Munich, Germany

A. Latz
Ulm University
Institute of Electrochemistry
Albert-Einstein-Allee 47, 89081 Ulm, Germany

by calendering, that is, pressing between two rotating steel cylinders, is the established standard, while isostatic or uniaxial pressing is used for laboratory-scale pellet and solid-state battery production. Besides the consolidation effect caused by pressing, large external and internal forces can lead to undesirable effects, such as the pressing of lithium metal into separator pores.[3–5] A recent interlaboratory study by Ohno et al. pointed out that in solid electrolyte research, no uniform protocol for fabricating and measuring ion conductors exists. The study found that both the pelletizing pressure and stack pressure (pressure during measurement) influence the reported ionic conductivities, especially for mechanically soft thiophosphates.[6] We refer to stack pressure as the pressure constantly applied during operation by the cell housing or an external system. Although the influence of (stack) pressure on the ionic conductivity of materials like silver halides,[7–10] lithium borohydrides,[11,12] lithium metal oxides (e.g. lithium lanthanum titanate (LLTO)[13] and Li-β-alumina[14]), as well as sodium ion conductors (e.g. Na_3SbS_4[15] and Na_3PS_4[16]) have been studied, data for lithium thiophosphates is still sparse. To classify the existing literature, two effects need to be distinguished. First, pressure can impact the state of sample densification. If the (crystalline) sample under study is not a single crystal, the relative density ρ_{rel}, that is, the ratio of the geometric density ρ_{geo} and the crystallographic density ρ_{cryst} normally is $0 < \rho_{rel} < 1$. While low ionic conductivity is commonly expected at low relative density, higher relative densities promise higher ionic conductivity, because the amount of non-contributing voids between solid electrolyte particles is lower and particle contacts are increased. Kodama et al. imaged the compression of Li_6PS_5Br particles using X-ray computed tomography (CT) and used the 3D information to simulate the evolution of ion transport in the sample at different pressure levels.[17] They concluded for increasing pressure that the particles are crushed and fill empty cavities, which is similar to a sintering process at room temperature. Following this work, Kodama et al. used morphological descriptors such as sphericity and contact ratio measured on individual particles via X-ray CT. They showed that the increased ionic conductivity was due to the collapse of the cavities and the increase in contact area with increasing pressure.[18] While these studies focused on the compression of a powdered sample—a microstructural phenomenon[15,17–20] —other research groups focused on the atomistic effect of pressure on ionic conductivity.[8–14,16,21,22] Although often neglected, solids can be elastically compressed by shrinkage of the unit cell, resulting in smaller bond lengths and different bond angles. All these effects alter the dynamics of ion migration by changing the volume required for migration between different sites. This fundamental thermodynamic effect is described by the activation volume which we will discuss in more detail further below.

Figure 1 compiles literature data on some lithium, sodium, and silver ion conductors. The hollow data points represent measurements where the pressure on the powder sample was increased, thus compressing the sample into a pellet. The filled data points represent conductivity measurements made on preformed pellets (circle) or, in the case of Li-β alumina, on a single crystal (diamond). While the conductivity data measured on pre-pressed pellets mostly show a linear behavior of $\ln(\sigma)$ with pressure, the measurements starting with unpressed powder show a different trend. With increasing pressure, the ionic conductivity increases

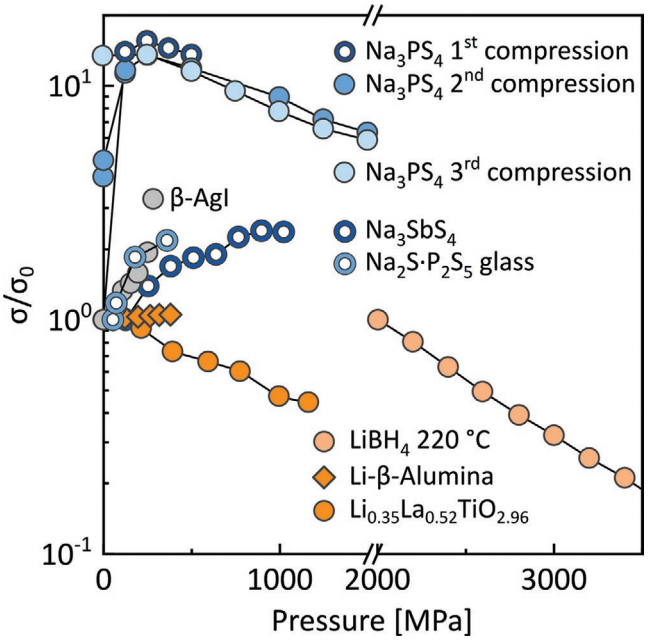

Figure 1. Pressure behavior of Na_3PS_4,[16] Na_3SbS_4,[15] $Na_2S{\cdot}P_2S_5$ glass,[19] β-AgI,[8] $LiBH_4$,[12] Li-β-alumina,[14] and $Li_{0.35}La_{0.52}TiO_{2.96}$[13] (LLTO) ion conductors extracted from literature. The conductivities σ were normalized to the conductivity σ_0 measured at the lowest available pressure to better compare literature data that is otherwise several orders of magnitude apart.

rapidly at first, eventually approaching a maximum. For Na_3PS_4, the pressure behavior after reaching the maximum in conductivity is similar to the behavior of pre-compressed samples.[16] Famprikis et al. explained this behavior with two regimes, an extrinsic compaction regime at low and an intrinsic activation volume regime at high pressure.[16] However, the extrinsic regime for the second and third compression cycle exhibits the low pressure characteristics of the first cycle, indicating detrimental electrode-sample contacts at low pressure. In the extrinsic, low pressure region, the compaction of the powder dominates,[16] while at higher pressure the effect of unit cell compressibility, as observed in β-AgI,[8] $LiBH_4$,[12] Li-β-alumina,[14] and LLTO,[13] dominates.

In this study, we investigate the effect of pelletizing and stack pressure on the powder compression of the $Li_{10}GeP_2S_{12}$-like ion conductor tetragonal Li_7SiPS_8 (t-Li_7SiPS_8), and show how (stack) pressure affects pellet density and sample impedance. An analysis of the mechanical response of the powder under uniaxial loading shows that the t-Li_7SiPS_8 thiophosphate sample follows the empirical Heckel equation for powder compression, enabling the distinction of different compaction regimes. Furthermore, we show that particle size influences the measured compression mechanics and ionic conductivity, but not the derived activation volume. The transport properties and positive activation volume of t-Li_7SiPS_8 are supported by ab initio molecular dynamics calculations. Finally, we demonstrate how image-based analysis of particle size and morphology, in conjunction with simulation using the discrete element method and subsequent finite volume analysis of the microstructure, helps to gain insight into the pellet formation process by only using geometric information as an input.

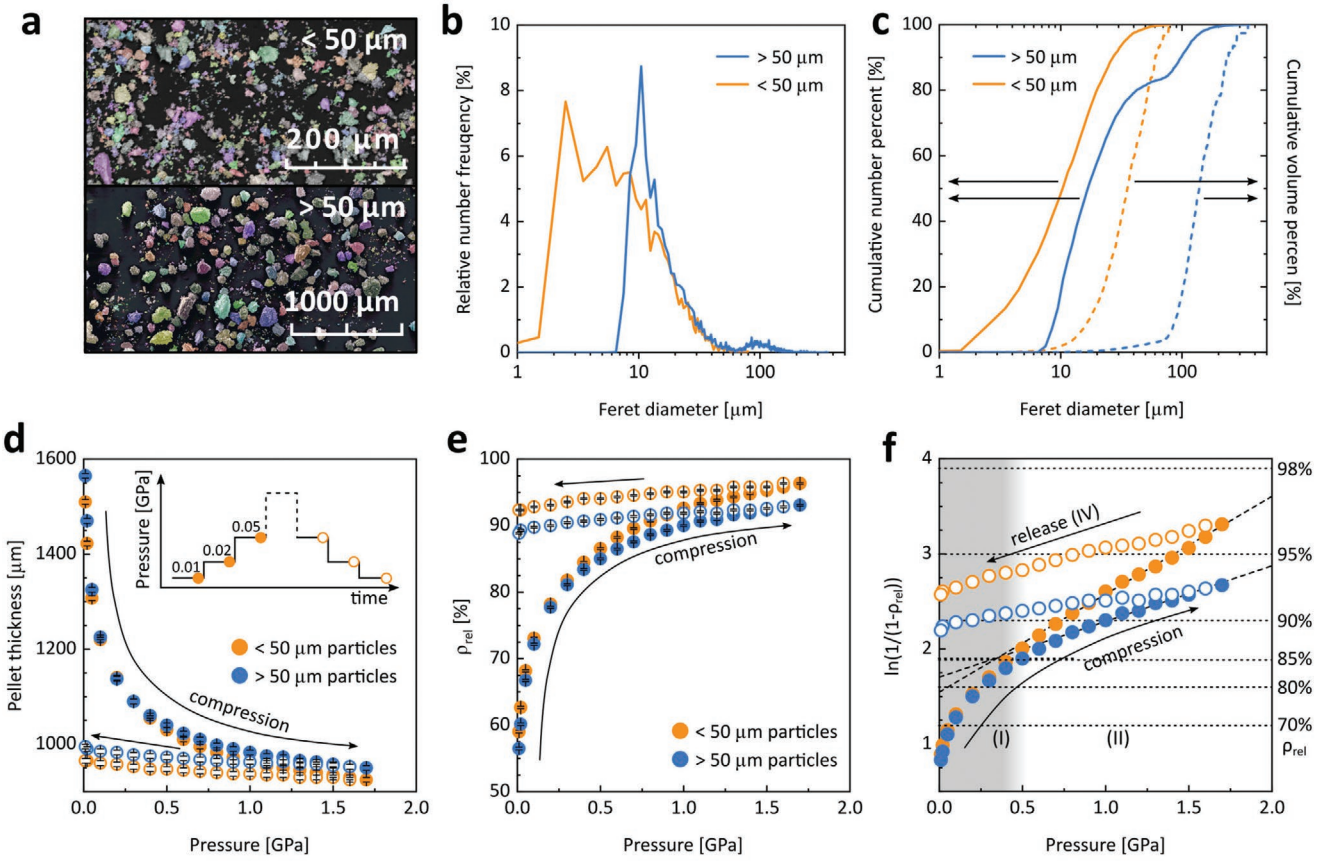

Figure 2. a) False color SEM image of the two *t*-Li_7SiPS_8 sieving fractions. b) Relative number fraction of *t*-Li_7SiPS_8 particle sizes (expressed as the Feret diameter). c) Cumulative number- (straight line) and volume-based (dashed line) PSD. The volume-based distribution curves were calculated based on the Feret diameter. d) Evolution of pellet thickness and e) pellet relative density of *t*-Li_7SiPS_8 sieving fractions under pelletizing pressure. The insert in (d) schematically depicts the experiment. The filled data points indicate increasing pressure, while the hollow points indicate the release sweep. f) "in die" Heckel plot analysis for the two sieving fractions. The dashed lines indicate the linear regime, while the dotted lines aid to estimate the relative density of the sample. The gray and white areas correspond to the regions in which particle rearrangement and (agglomerate) fragmentation (I), as well as plastic deformation of the particles (II) dominate the compression sweep.

2. Results and Discussion

2.1. Mechanical Stages of Powder Consolidation

First we investigate the macroscopic mechanical response of *t*-Li_7SiPS_8 powder to the applied pressure as a function of particle size. To this end, we have prepared two particle size fractions by sieving with a 50 µm mesh-size sieve. We refer to the Supporting Information for more details on domain and particle size. The fraction passing the sieve is denoted as the <50 µm fraction, while the powder remaining in the sieve is denoted the >50 µm fraction. We determined the (secondary) particle size distribution (PSD) of the two fractions by analyzing scanning electron microscopy (SEM) images with ImageJ[23] plugins[24,25] (see **Figure 2**a). The procedure is included in the Supporting Information file along with a flowchart (Figure S2, Supporting Information), example images (Figure S3, Supporting Information), and SEM images (Figures S4 and S5, Supporting Information). Additionally, information about particle morphology is included in the Supporting Information (Figures S7 and S8, Supporting Information). Figure 2b shows the relative number fraction of binned (1 µm) particle sizes for both samples. The <50 µm sample follows a monomodal PSD, while the >50 µm sample shows a bimodal PSD. Despite the fact that small particles dominate the number-based PSD for the >50 µm sample, the bulk of the sample consists of >50 µm particles, as shown in the volume-based PSD (see Figure 2c, blue dashed line) and indicated by the D_{10} = 89 µm value. The D_{10}, D_{50}, and D_{90} values for the PSDs are summarized in Table S1 and S2 in Supporting Information.

The evolution of the pellet thickness with (uniaxial) pelletizing pressure of the two *t*-Li_7SiPS_8 powder samples is shown in Figure 2d. A scheme representing the experimental procedure is depicted using an insert in Figure 2d. Increasing the pressure leads to a fast initial decrease in pellet thickness that saturates at a thickness where the relative density of the pellet approaches 100%. Upon releasing the pressure, the pellet thickness increases and the pellet density decreases by about 4%, as depicted in Figure 2e. The <50 µm sample has a higher initial density and results in a denser pellet after pressing at 1.7 GPa compared to the >50 µm sample. To better understand the compaction mechanism of *t*-Li_7SiPS_8, the empirical Heckel equation[26] derived from the compaction of metal powders was applied to the "in die" pressure-density data. Despite the large number of published mathematical descriptions of powder compaction, the Heckel equation is still widely used in particle technology and

pharmaceutics. Assuming that the functional form of pellet formation is formally analogous to a first-order chemical reaction, the Heckel equation takes the form:

$$\ln\left(\frac{1}{1-\rho_{\mathrm{rel}}}\right) = Kp + A \quad (1)$$

where ρ_{rel} is the relative density of the specimen at pressure p. K and A are the slope and y-intercept of the linear region of the Heckel plot. Additionally, Heckel plots can be classified into "in die" and "out of die" measurement conditions. While "in die" plots represent data measured during compaction under pressure, "out of die" plots are generated from data measured at very low or zero pressure.[27]

Generally, three different states of powder compression regimes can be identified in "in die" Heckel plots, if sufficiently high pressures are applied.[27,28] A schematic "in die" Heckel plot is given in Figure S9a, Supporting Information. Notably, the three compression regimes may merge and different consolidation mechanisms may prevail at the local level, depending on the local density and the availability of voids. In regime I, individual particles rearrange until they are held in place by interlocking with neighboring particles or the die wall. To some extent, agglomerates may also fragment when the capability for elastic and inelastic deformation of the agglomerate is exhausted. Fragmentation depends on the particle size and critical stress intensity factor that describes the stress needed for crack propagation.[29] This adds to the increase of the relative density as voids are filled and is indicated by the nonlinear regime in the Heckel plot. Figure 2f indicates that regime I dominates the compression up to 0.5 GPa and that both sieving fractions behave comparably in this first compression stage.

Once (fragmented) particles are locally fixed, elastic and plastic deformation of a majority of particles takes place. This phase of the compression is referred to as regime II and dominates for pressures above 0.5 GPa. It can be recognized in Figure 2f as a linear region of the Heckel plot, following Equation (1). Once local stresses exceed the elastic limit of an individual particle, irreversible mechanical changes, either by plastic deformation or fragmentation, lead to further consolidation.[27,28] Whereas brittle materials tend to break into smaller pieces that can fill voids, softer materials such as thiophosphates may exhibit plastic deformation.[30] While similar in regime I, the two PSD samples exhibit different slopes in regime II. The reciprocal of the slope K can be interpreted as the mean yield pressure P_y of the material, which describes the stress required for plastic flow.[28,30–32] For the <50 µm sample the calculated P_y from the "in die" data is smaller (0.95(3) GPa) than that for the >50 µm sample (1.65(3) GPa), indicating easier plastic deformation for the sample with the smaller particle size. The mean yield pressure calculated from "out of die" data shown in Figure S9d, Supporting Information, is higher for both PSDs compared to the "in die" data, but still follows the trend of higher P_y for larger PSD. Lower mean yield strength can indicate lower fracture strength of individual particles, leading to more facile deformation under pressure and thus higher compressibility.[33]

In the final compression stage, regime III starts to dominate when almost all pores are eliminated and the density is close to 90–95%.[34] At this stage, the individual particles are no longer distinguishable (see Figure S10d, Supporting Information), and the pellet behaves more like a single body that deforms elastically as the pressure increases.[35] In the Heckel diagram, this condition is usually visible as an upward curvature with increasing pressure, as shown in the schematic Heckel plot in Figure S9a, Supporting Information.[35] For t-Li_7SiPS_8, no distinct deviation from the linear regime is observed at high pressure, indicating that the pressure is not sufficient to enter regime III. However, the comparison of "in die" and "out of die" Heckel plots (see Figure S9d, Supporting Information) clearly depicts elastic contributions in regime II. Since the "out of die" curve is measured at a low stack pressure of 0.01 GPa, where almost no additional elastic recovery is to be expected, the difference between "out of die" and "in die" data is attributed to the elastic deformation of the pellet.[36] Hence, the typical Heckel regimes II and III cannot be visually differentiated for t-Li_7SiPS_8 in the "in die" analysis within the measured pressure range, but pellet elasticity is observed as the difference between "in die" and "out of die" curves.

The release of pressure decreases the density and is commonly described as regime IV of fast elastic recovery/relaxation into the "final" pellet size.[37] The <50 µm sample exhibits a larger elastic recovery compared to the larger sized sample, as indicated by the steeper slope upon pressure release (see Figure 2f). This agrees well with the compression sweep that yielded a larger difference between the "in die" and "out of die" P_y for the <50 µm sample compared to the >50 µm sample.

The pellet formation process, which includes elastic and more importantly plastic deformation, leads to microscopic defects in the pellet body. SEM images taken on pellets compressed at 1.7 GPa, depicted in Figure S10b,c, Supporting Information, show signs of cracks on the scale of tens of micrometers after release from the die. While the cracks are caused by the plastic deformation process and can be restrained by elastic deformation at higher pressure, they appear when the pressure is relieved.

2.2. Influence of Pelletizing Pressure on the Ionic Conductivity of t-Li_7SiPS_8

The nontrivial mechanical response of the powder samples, as described in the previous section, clearly affects the ionic conductivity. **Figure 3** shows the evolution of the ionic conductivity of the two different t-Li_7SiPS_8 samples with increasing and decreasing pressure. Exemplary Nyquist plots are shown in Figure S11, Supporting Information. At 0.01 GPa, the untreated and uncompacted powder samples show an ionic conductivity of 0.3 mS cm^{-1} for the <50 µm and 0.7 mS cm^{-1} for the >50 µm sample. This difference is likely due to contact effects between individual particles: In the <50 µm sample more individual particles are present in the same total sample mass. Consequently, this results in more microscopic grain-to-grain contacts (secondary particles), thus possibly leading to a higher resistance for ionic conduction due to more unfavorable grain-to-grain orientations. Harm et al. have shown that in the glass-ceramic t-Li_7SiPS_8 intra- and intergrain diffusion processes are mixed, with a higher diffusivity on a shorter (intergrain) length scale.[38] A recent study of Ates et al. also points out that grain boundaries impact the ionic conductivity more than particle porosity and tortuosity.[39] As the pressure increases, this trend

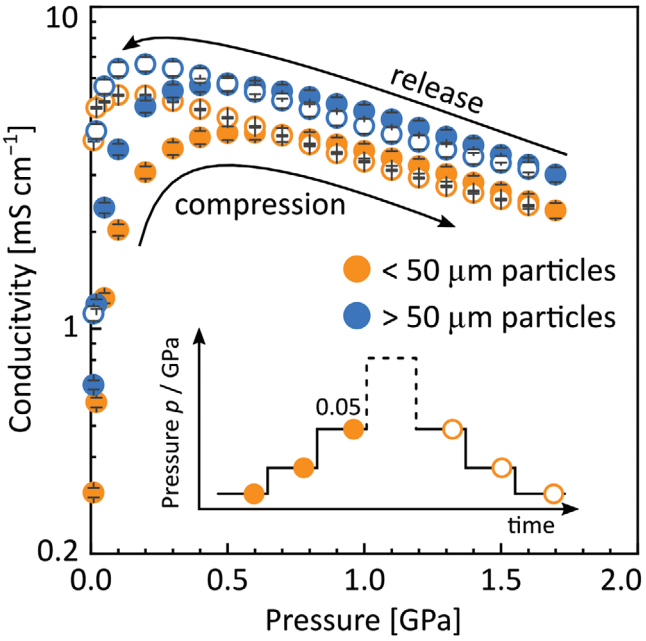

Figure 3. Evolution of ionic conductivity with applied uni-axial pressure (first cycle). Orange and blue circles represent <50 µm and >50 µm particle size fractions, respectively. Hollow and filled circles denote impedance measurements performed on increasing and decreasing the applied pressure (see inserted scheme).

of lower ionic conductivity for the smaller PSD continues and is observed for all measured pressures.

Both samples show a sharp increase in σ with increasing pressure until a maximum of 4.1 mS cm^{-1} is reached for the small and 5.7 mS cm^{-1} for the large particle sizes (both at 0.5 GPa). Although the smaller batch is more densely packed (Figure 2b), the ionic conductivity is lower, suggesting that detrimental particle-particle contacts dominate the conductivity (vide supra). After reaching a maximum ion conductivity, both samples show a nearly linear decrease in $\ln(\sigma)$ with pressure. Upon pressure release, σ increases until it reaches a maximum of 5.3 mS cm^{-1} (<50 µm) and 6.6 mS cm^{-1} (>50 µm) at about 0.1–0.2 GPa. At the lowest applied pressure (0.01 GPa), the pelletized samples exhibit an ionic conductivity of 3.8 mS cm^{-1} (<50 µm) and 1.1 mS cm^{-1} (>50 µm). After repeating the compression and release procedure, the ionic conductivity at 0.01 GPa is 4.4 and 2.1 mS cm^{-1} (not shown) for the small and large fractions, respectively. While the smaller PSD sample shows only a slight improvement on the second compression cycle, the larger PSD fraction almost doubles in ionic conductivity (at 0.01 GPa). Subsequent compression/release cycles are expected to improve the pellet/electrode interface by plastically deforming the top particles, thus smoothing the surface. A similar behavior for the second and third compression cycle was observed for Na_3PS_4 (see Figure 1).[16] We draw two conclusions from the observations so far. First, the ionic conductivity of *t*-Li_7SiPS_8 powder batches with larger particle fractions is higher than for the smaller particle fraction, regardless of the compression stage during pelletizing. In addition, the >50 µm is more sensitive towards the release of pressure. Relative pellet density has a smaller influence on ionic conductivity than particle size when the pellet is formed. Therefore, higher pellet density, as observed for the <50 µm sample, is not the only influencing factor for higher conductivity, as measured for the >50 µm sample. Our metadata analysis of Ohno's study about the reliability of conductivity measurements on argyrodites also shows that pellet density only weakly correlates with ionic conductivity.[6] For more information, please refer to the Supporting Information. Second, the ionic conductivity at very low pressure (release sweep) is affected by factors other than pellet compression. As the contact pressure decreases, the contact resistance at the interface between the electrode and the sample has an increasing effect on the measured impedance, and is sensitive toward the PSD. This low pressure effect and possible explanations are presented in a later section.

2.3. Influence of Activation Volume on Ionic Conductivity

As described before, the non-linear evolution of ionic conductivity of a powder sample under increasing pressure is a result of two effects. The microscopic effect (see above) is governed by powder compression and pellet formation at low pressures, and the atomistic effects of molar volume compression dominates at high pressures. To better understand these atomistic effects, let us first analyze the Li transport properties of *t*-Li_7SiPS_8 in the absence of pressure.

Harm et al.[38] have reported a high total ionic conductivity of 2 mS cm^{-1} and activation energy of 0.27 eV for *t*-Li_7SiPS_8. The activation energy is in line with calculated migration barriers of 0.22 eV for 1D ion migration along the *c* direction and 0.28 eV for 3D migration obtained from bond valence sum simulations[40–42] as illustrated in **Figure 4**a. This anisotropy is confirmed in ab initio molecular dynamics (AIMD) simulations: The diffusion coefficient along the *c* direction has a lower activation barrier and is found to be approximately four times higher than along the *a*/*b* directions (see Figure S17, Supporting Information). For more details on the AIMD simulations, we refer to the Supporting Information.

At pressures above 0.5–0.7 GPa, the linear decrease of $\ln(\sigma)$ in Figure 3 reveals that the effect of molar volume compression dominates the pressure dependence. In other words, the pressure leads to an elastic compression of the formed pellet and thus the material. To illustrate how this affects the Li migration, AIMD simulations have been performed based on structural models, whose cell parameters have been uniformly rescaled (see Figure 4b). Based on the calculated elastic constants (see Supporting Information), the estimated pressures of these calculations are 0.8 and 1.7 GPa for the utilized scaling factors *f* of 0.99 and 0.98, respectively. The resulting Li mean-squared-displacements (MSD) indicate that the diffusion is lowered in compressed cells.

The pressure dependence of the ionic conductivity is connected to the activation volume ΔV. The activation volume can be formally expressed by the following equation:

$$\Delta V = k_B T \left(\left(\frac{\partial \ln(\sigma_0)}{\partial p} \right)_{T,N_i} - \left(\frac{\partial \ln(\sigma)}{\partial p} \right)_{T,N_i} \right) \quad (2)$$

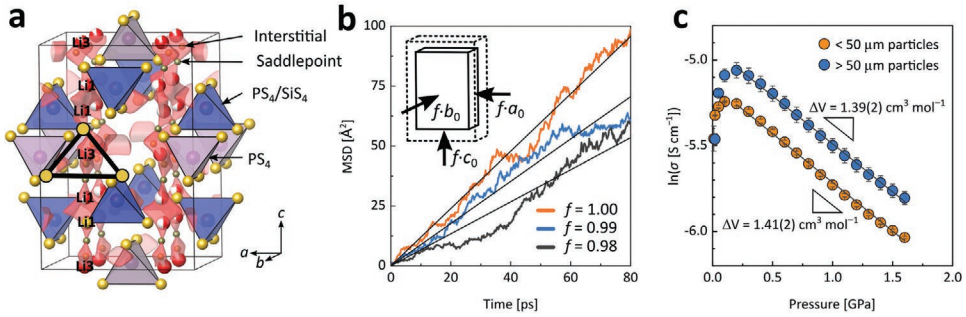

Figure 4. a) Crystal structure of *t*-Li_7SiPS_8 with the bond valence sum iso-energy landscape in red, indicating favorable 1D conduction channels along the *c* direction. The black triangle depicts the bottleneck spanned by three sulfur atoms. b) Li MSD from AIMD simulations at 700 K for different cell volumes of *t*-Li_7SiPS_8. Linear fits of Li MSD are depicted as straight grey lines. c) Natural logarithm of ionic conductivity of *t*-Li_7SiPS_8 from the experiment with pressure. The fitted slope is depicted as a black line. The data points and error bars represent the average and standard deviation of three (<50 µm) and two (>50 µm) consecutive pressure-release sweeps.

We refer to the Supporting Information for a more detailed derivation of Equation (2). The pressure dependence of the pre-exponential factor σ_0 is small (less than 10% of the second term in Equation (2))[11,16,43–47] as verified with AIMD simulations for $Li_{10}GeP_2S_{12}$.[48] Therefore, we can simplify Equation (2) to:

$$\Delta V \approx -k_B T \left(\frac{\partial \ln(\sigma)}{\partial p} \right)_{T,N_i} \tag{3}$$

A more accurate approximation of the activation volume, which was derived specifically for cubic crystal systems, is presented in the Supporting Information. For *t*-Li_7SiPS_8, we will refer to the simplified definition of the activation volume as given in Equation (3).

While activation energy is generally understood as an activation barrier to be overcome, the activation volume has a different physical meaning. In ion-conducting solids, the ions require a certain volume V_m for local migration from one site to another, that is the space needed at the saddle point, while the (anionic) sublattice provides a free volume V_f. The activation volume ΔV is defined as the difference between V_m and V_f:[14,16,47,49]

$$\Delta V = V_m - V_f \tag{4}$$

Thus, a non-zero activation volume indicates a mismatch between the free volume of the structure and the volume required for ion migration. If an ion must migrate through a bottleneck too narrow for its size, the lattice locally expands, which is described by a positive activation volume.[14,16,49] In some cases, ΔV is negative and enhanced ion transport with increasing pressure is observed.[14,50]

Based on the data shown in Figure 4b we estimate an activation volume of 1.7–2.0 $cm^3\ mol^{-1}$. However, more extensive simulations would be required to accurately verify the computed activation volume. Nevertheless, these results align well with the findings of Fu et al. for tetragonal $Li_{10}GeP_2S_{12}$ (LGPS).[48] Through structural relaxation and AIMD simulation, they calculated an activation volume of 2.17 $cm^3\ mol^{-1}$ and found a (positive) linear correlation of lithium ion diffusivity with the volume of the unit cell and the "neck size" of the migration path, similar to the triangle spanned by sulfur ions from tetrahedral units as drawn in Figure 4a.[48]

In addition to simulating the effect of cell compression via AIMD calculations, we extracted the activation volume based on experimental data. A small increase in pellet density is observed in the second (and third) compression sweep, which affects the calculated ionic conductivity. To exclude further consolidation effects (deviation from linearity), only the release sweeps were considered for evaluating the activation volume. The activation volume resulting from fitting the linear range in Figure 4c is approximately 1.4 $cm^3\ mol^{-1}$ for both size fractions, indicating that the activation volume is independent of particle size and morphology and is an intrinsic material property. The magnitude of the activation volume is in line with our simulations as well as with other lithium and sodium solid electrolytes.[16]

The positive sign of ΔV indicates that the *t*-Li_7SiPS_8 host structure must expand locally to accommodate a lithium ion at the saddle point of ion migration.

2.4. Pressure Effect on Crystallinity

In addition to the effect of activation volume, phase transitions, as in $LiBH_4$,[11,12] can also lead to changes in the impedance of a sample under pressure. However, phase transitions usually manifest in jumps in one or more properties of a material, like volume expansion, change in crystal structure, or a change in the transport properties. The impedance shows no such jump, hence a pressure induced first-order phase transition can be ruled out. Li_7SiPS_8 is a glass-ceramic[38] in which a side phase limits the ionic conductivity. The side phase was assumed to be amorphous due to the absence of additional Bragg peaks.[38] We measured ^{31}P-solid-state NMR to determine the amount and change of the side phase in the untreated and pressed samples. The ^{31}P MAS NMR spectra are shown in Figure S12a, Supporting Information. The pristine sample has 8.2 to 9.0 wt% side phase, while the sample pressed at a pelletizing pressure of 1.7 GPa has a weight fraction of 9.7 to 10.2% side phase. For samples with larger particles, the weight fraction of the side phase is slightly higher than for the fraction with smaller particles. However, this difference is minute and unexpected since both particle size fractions were recovered from the same sample. The difference in the side phase is thus probably due to small differences in the homogeneity of the sample or to

fitting errors. The increase of around 1–1.5% after pressing could be due to stress from plastic deformations during pellet formation. In particular, where the material flows plastically into voids, the crystalline domains could be subject to greater shear forces, resulting in sliding of lattice planes and thus loss of long-range order. This is reflected in a significant peak broadening (FWHM) for the *t*-Li_7SiPS_8 signals of the pressed samples compared to the unmodified powder (see Figure S12b, Supporting Information). Additionally, the peaks associated with the amorphous side phase exhibit broadening, indicating a wider range of chemical environments for the side phase, likely caused by the stress during compaction.

2.5. Influence of Stack Pressure on the Ionic Conductivity of *t*-Li_7SiPS_8

As described above, the ionic conductivity of *t*-Li_7SiPS_8 pellets formed at high pressure is lower at low stack pressure. This might be caused by a higher surface roughness, as indicated by the cracks observed in the SEM image in Figure S10b, Supporting Information, leading to lower apparent conductivity of the sample due to current limiting effects. To mitigate this problem, noble metals are usually sputtered onto the pellets to better distribute the current load. Since sputtering is not available for every lab, we systematically investigate how improving the sample-electrode contact can be reached by varying the stack pressure. To this end, we programmed a pressing routine that includes impedance measurements at 0.01 and 0.1 GPa stack pressure in between pelletizing steps at variable pressure. These stack pressures are close to those used in spring-loaded setups such as Swagelok cells or threaded rod press cages, and represent the pressure under which the lowest and highest ionic conductivity was measured previously in the pelletizing pressure experiments. Additionally, any influence of the activation volume on conductivity can be neglected at these pressures.

Figure 5 shows the evolution of ionic conductivity of *t*-Li_7SiPS_8 for both particle size fractions at 0.01 and 0.1 GPa stack pressure after being compacted at increasing pelletizing pressures (*x*-axis in Figure 5). It reveals that the trend toward higher ionic conductivities for the >50 µm compared to the <50 µm sample also holds for the stack pressure test. We find that measured ionic conductivity depends not only on the compaction state of the pellet, expressed here by the pelletizing pressure, but also on the pressure applied to the pellet during the impedance measurement. The initial increase in conductivity up to a pelletizing pressure of 0.3–0.5 GPa is observed for both contact pressures and can be explained by the rearrangement and fragmentation of the particles, as previously described in the Heckel plot analysis. However, at low stack pressure, a plateau followed by a further increase in conductivity is observed for both size fractions of *t*-Li_7SiPS_8, while at a higher stack pressure of 0.1 GPa, the measured impedance after the initial regime is almost independent of the pelletizing pressure. Cronau et al. observed a similar behavior for glass-ceramic and micro-crystalline Li_6PS_5Br, where a stack pressure of at least 0.05 to 0.1 GPa is needed to achieve low sample impedance.[20]

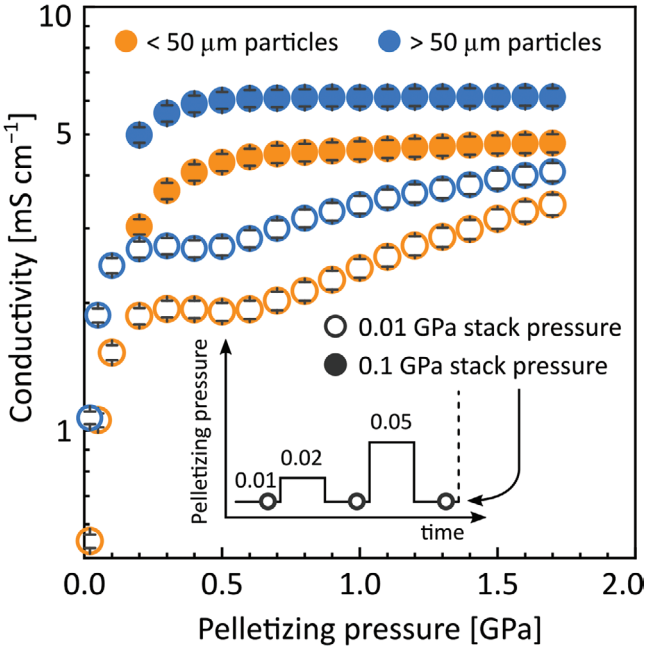

Figure 5. Evolution of ionic conductivity with applied uniaxial stack pressure. Hollow and filled circles represent EIS measurements performed at a stack pressure of 0.01 and 0.1 GPa, respectively. The particle size fractions of <50 µm and >50 µm are depicted in orange and blue. The inserted scheme describes the measurement procedure of EIS measurements at a fixed stack pressure after pressing at variable pelletizing pressures.

Here, two effects could explain the observed difference between high and low stack pressure. First, higher stack pressure could result in smoother sample-electrode interfaces, which reduces the interfacial impedance. At very low or zero stack pressure, a pronounced surface roughness is expected. Figure S10b, Supporting Information shows the pellet surface (prepared at 1.7 GPa) imaged by SEM. Although the surface seemed to be smooth when inspected with bare eyes, it exhibits lots of cracks on the scale of tens of micrometers, thus is microscopically rough. A higher stack pressure likely prevents the surface crack opening. As a second effect, the release of pressure down to 0.01 GPa could increase the impedance of the particle-particle contacts. This effect might be larger at low pelletizing pressures where particle binding, that is, the formation of a solid pellet, is not fully achieved. At higher pelletizing pressures, the impedance between grains should decrease and approach bulk conductivity. As can be seen in Figure 5, the conductivity measured at 0.01 GPa stack pressure approaches the conductivity obtained at higher stack pressure, but is still lower even at the highest pelletizing pressure. There, the higher elastic deformation present at higher stack pressure prevents internal crack opening and explains the higher conductivity. This suggests that the mechanical response, as well as the interface contact and the internal crack opening (see Figure S10, Supporting Information) contribute to the unique features of the conductivity evolution at 0.01 GPa stack pressure shown in Figure 5. The higher elastic compression at a higher stack pressure can prevent crack opening and ensures a better electrode contact.

This agrees well with the finding of Cronau et al. who have reported sufficient particle binding in glass-ceramic Li_6PS_5Br at a pelletizing pressure of at least 0.4 GPa.[20] They also suggest to sputter metal electrodes onto the pellet if maintaining a higher stack pressure during the measurement is not possible.

2.6. Simulation of Powder Compression

The influence of *t*-Li_7SiPS_8 powder compression on the conductivity was further investigated by simulating the pellet compression using a discrete element method (DEM) simulation followed by electrochemical analysis of the obtained pellet microstructures using a finite volume analysis (FVA).

The DEM model, as described in the methods section in detail (see Supporting Information), is implemented in the in-house multi-physics research code BACI[51] and used to perform the powder compacting simulations. To parameterize the simulation model, information from the experimental investigations concerning the material, the geometric dimensions of the pelletizing experiments, and the PSD is necessary. Relevant parameters that have been used for the DEM simulations are listed in Table S5 in the Supporting Information. A domain with a base of 210 × 210 µm^2 and a height of 1700 µm was constructed and loaded with 9591 particles for the simulations. Obviously, the lateral dimensions of the pellet in the experiment are significantly larger. However, we chose the lateral dimension in the simulation such that the discrete particle distribution is reasonably close to the experimentally determined one, and such that we can assume that all relevant interaction effects are properly represented. To account for the larger dimensions in reality, periodic boundary conditions where applied in the lateral directions (x – and y –direction) to actually extend the area infinitely, whereas the correct pellet thickness in z –direction is exactly captured. Furthermore, the required PSD of the synthesized material was measured using SEM image analysis as described before and in more detail in the Supporting Information.

Figure 6a shows the particle distribution of the <50 µm *t*-Li_7SiPS_8 sample as a 1 µm bin histogram of the Feret diameter (see definition in the Supporting Information). The histogram was fitted with a gamma distribution with a = 1.94431 and b = 7.04802, and the distribution parameters were used as input for the parameterization of the DEM model.

At the end of the particle compacting simulations, we extracted the positions and radii of the particles defining the resulting microstructures, serving as an input to the FVA, for which voxel-based structures were generated. Using the finite volume implementation battery and electrochemistry simulation tool (BEST)[52,53] effective ionic conductivities of the compressed electrolyte pellets were calculated by simulating the steady state current distribution in the sample for an applied voltage difference. In the first simulation scenario, the bulk conductivity was reduced with the effect of activation volume at constant stack pressure, while in the second scenario the bulk conductivity was reduced with increasing variable pressure. Details concerning the applied FVA method can be found in the Supporting Information.

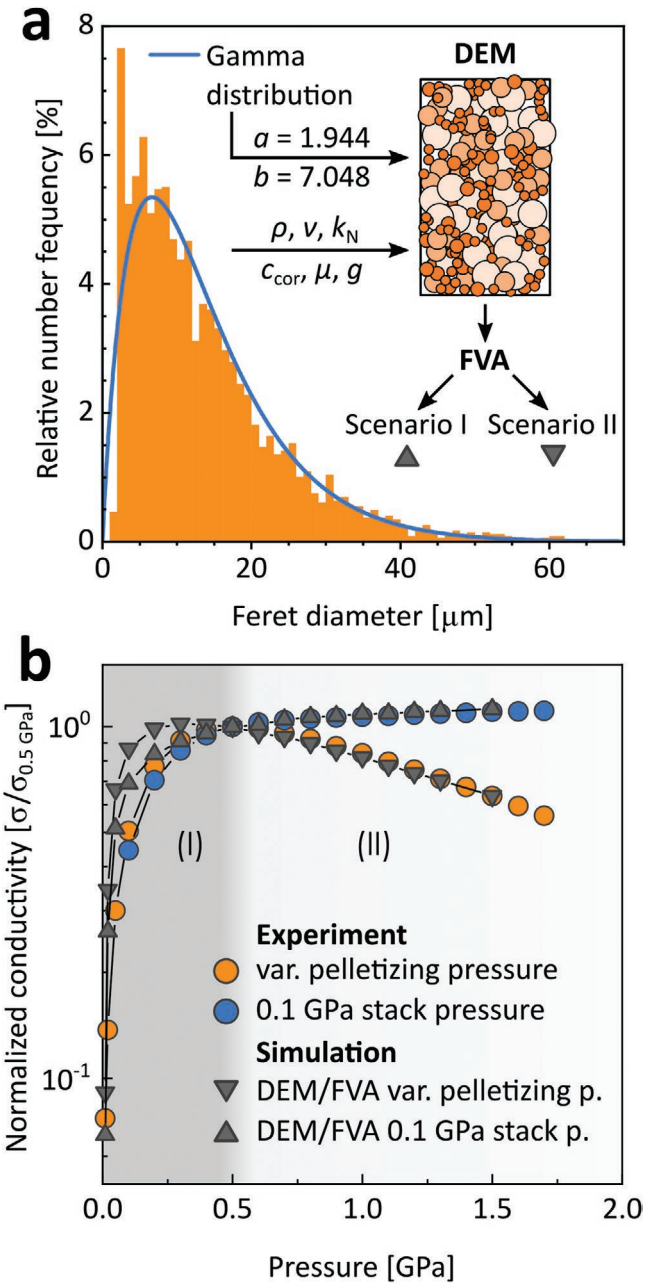

Figure 6. a) Histogram plot of Feret diameter distribution of *t*-Li_7SiPS_8 (<50 µm) with gamma distribution function fit in blue. A workflow scheme for the DEM/FVA is depicted as an insert. b) Normalized ionic conductivity from varying pelletizing pressure (orange) and constant stack pressure (0.1 GPa, blue) experiment as a function of variable compression pressure. For the DEM/FVA, the pressure axis relates to the experimental pellet thickness, that was used for parametrization. The activation volume effect was considered in both scenarios, however it is almost negligible in the 0.1 GPa stack pressure scenario (upward triangle) compared to the variable pressure scenario (downward triangle). The experimental conductivity was normalized to the value at 0.5 GPa. At this pressure, the maximum ionic conductivity in the pelletizing pressure experiment was reached.

The normalized ionic conductivity determined from the experiment under variable pressure and constant stack pressure (0.1 GPa) is shown in Figure 6b. In addition, Figure 6b includes

the results from the DEM/FVA-simulations for both scenarios. Since the conductivity values are normalized, the simulated values do not depend on the assumed bulk conductivity but only on the geometric properties of the input structures. Qualitatively, the simulations show good agreement with the experimental results, capturing the observed effects for both the measurements at constant and variable stack pressure. The applied external pressure results in the compaction of the pellet by rearrangement and deformation of the particles. The larger contact surface between the particles (see Figure S13 in the Supporting Information), which is modeled by particle overlapping in the DEM, leads to better transport pathways in the electrolyte pellet and a consistently increasing effective conductivity for the first scenario resembling the stack pressure experiment. The good agreement with the experimental measurement shows that the changes of the electrolyte microstructure are captured correctly by the DEM-simulations. For the second case considering the increasing activation volume effect with pressure, the decrease in bulk conductivity with increasing external pressure in the FV-simulations leads to a drop in effective conductivity after reaching a maximum at moderate pressures. The resulting slope corresponds to the experimental values and indicates that the reduction of ionic conductivity described by the activation volume is indeed the prominent effect at variable pelletizing pressure. However, for small pressures in regime (I) the simulated conductivities are consistently higher than the experimental values for both simulation cases. The observed deviation from the experiment can be attributed to the difference between the DEM model consisting of perfect spheres and the powder, which consists of particles that are not perfectly spherical. Consequently, friction and contact resistance effects stemming from the different particle morphology are not fully taken into account in the DEM model. Furthermore, grain boundary resistances, which could be higher for small external pressures, are not included in the FV-simulations. A more detailed discussion on particle morphology is presented in the Supporting Information.

3. Conclusion

In this study, we investigate the macroscopic (i.e., microstructural) and microscopic (i.e., atomistic) effects of pelletizing and stack pressure on the ionic conductivity of *t*-Li_7SiPS_8, and support our findings by a comprehensive multiscale simulation study of powder compression. Our study reveals a profound influence of particle morphology and PSD on the pressure behavior of thiophosphate solid electrolytes. The "in die" (variable pelletizing and stack pressure) and "out of die" (variable pelletizing and constant stack pressure) Heckel analysis suggest that the PSD affects both relative pellet density and the mean yield pressure, and thus the plastic deformation of particles, as well as the elastic recovery. As a consequence, the PSD also has subtle effects on the fraction of amorphous side phases in this thiophosphate glass ceramic, as well as surface and internal crack opening. In all experiments, pellets prepared from larger PSD powders consistently exhibit higher ionic conductivity, despite their lower density compared to pellets consisting of smaller particles. We conclude that a higher number of secondary particle-particle contacts are detrimental for the ionic conductivity of the investigated glass ceramic, which highlights the importance of particle size control to maximize ionic conductivity. This further implies that the PSD should be specified in order to increase the inter-laboratory comparability and reproducibility of conductivity measurements.

In contrast to the microstructural effects, the atomistic effect of elastic unit cell compression is not affected by the PSD of *t*-Li_7SiPS_8. We point out that this intrinsic effect should be considered in high-pressure impedance measurements, as the activation volume influences the conductivity under pressure.

The combination of DEM and FVA simulations is able to reproduce the experimental results both at pelletizing and variable stack pressure with high fidelity, confirming the combined effects of microstructure and activation volume on the effective conductivity. Based on our study, we expect samples with an optimized PSD to exhibit an improved mechanical compression response which translates into higher ionic conductivity, thus pinpointing additional handles to improve the performance of solid electrolytes.

To conclude, we summarize the following recommendations for determining ionic conductivities of solid-state ion conductors. To obtain comparable ionic conductivity values, the PSD should be comparable. We suggest using sieves to obtain a fraction with a well defined PSD. Additionally, the influence of pelletizing pressure should be carefully evaluated, as higher pressures can introduce plastic deformation and thus influence phase fractions, like the amount of amorphous side phase in glass ceramics, or lead to a loss in crystallinity. A pelletizing pressure of around 0.5 GPa and a stack pressure of 0.1 GPa are required for glass-ceramic thiophosphates to minimize interfacial resistance and maximize ionic conductivity. These values may well differ for other solid electrolytes with significantly differing elastic moduli. We further note that data measured under high pressure should be interpreted with care, as they can include the atomistic activation volume effect. The same is true for pellet densities, which only present a weak correlation with ionic conductivities. Overall, our study reveals the importance of pressure effects on ionic conductivity and puts forward best practices to ensure a more reproducible reporting of ionic conductivities, thus increasing inter-laboratory comparability of ionic conductivity results.

Supporting Information

Supporting Information is available from the Wiley Online Library or from the author.

Acknowledgements

The authors acknowledge financial support by the Max Planck Society, the German Federal Ministry of Research and Education (BMBF), projects 03XP0177B (MPI-FestBatt I), 03XP0430B (MPI-FestBatt II), 03XP0174D (TUM-FestBatt I), 03XP0435B (TUM-FestBatt II), 03XP0174C (DLR-FestBatt I), 03XP0435A (DLR-FestBatt II), 03XP0435C (TUDa-FestBatt II), the Center for Nanoscience (CeNS) and the Deutsche Forschungsgemeinschaft via the Cluster of Excellence e-conversion (EXC2089). The authors thank I. Moudakovski for solid-state NMR measurements, V. Duppel for SEM imaging, and M. Hofer (TU

Braunschweig) for measuring PSD with the LUMizer. The authors gratefully acknowledge the computing time and facilities provided by the Computer Service group at MPI-FKF as well as on the high-performance computer Lichtenberg at the NHR Centers NHR4CES at TU Darmstadt. The authors acknowledge support with computational resources by the state of Baden-Württemberg through bwHPC and the German Research Foundation (DFG) through grant no INST 40/575-1 FUGG (JUSTUS 2 cluster).

Open access funding enabled and organized by Projekt DEAL.

Conflict of Interest

The authors declare no conflict of interest.

Author Contributions

C.S.: Writing—original draft, formal analysis, conceptualization, investigation, methodology, visualization, writing—review and editing, project administration; C.P.S.: Formal analysis, conceptualization, investigation, methodology, writing—review and editing, software; A.N.: Formal analysis, conceptualization, methodology, writing—review and editing, software; M.C.: Methodology, writing—review and editing, software; M.S.: Investigation, formal analysis, methodology, writing—review and editing, software; S.H.: Resources; C.M.: Methodology, writing—review and editing, software; T.D.: Formal analysis, methodology, writing—review and editing, software; K.A.: Supervision, funding acquisition; A.L.: Supervision, funding acquisition; W.A.W.: Writing—review and editing, supervision, funding acquisition; B.V. L.: Conceptualization, writing—review and editing, supervision, funding acquisition.

Data Availability Statement

The data that support the findings of this study are available from the corresponding author upon reasonable request.

Keywords

all-solid-state batteries, impedance, ionic conductivity, particle size distribution, pressure, thiophosphates

Received: November 14, 2022
Revised: January 9, 2023
Published online: March 3, 2023

[1] Y.-G. Lee, S. Fujiki, C. Jung, N. Suzuki, N. Yashiro, R. Omoda, D.-S. Ko, T. Shiratsuchi, T. Sugimoto, S. Ryu, J. H. Ku, T. Watanabe, Y. Park, Y. Aihara, D. Im, I. T. Han, *Nat. Energy* **2020**, *5*, 299.
[2] J. Janek, W. G. Zeier, *Nat. Energy* **2016**, *1*, 16141.
[3] J. Doux, H. Nguyen, D. H. S. Tan, A. Banerjee, X. Wang, E. A. Wu, C. Jo, H. Yang, Y. S. Meng, *Adv. Energy Mater.* **2020**, *10*, 1903253.
[4] C. Hänsel, P. V. Kumar, D. Kundu, *Chem. Mater.* **2020**, *32*, 10501.
[5] C. Hänsel, D. Kundu, *Adv. Mater. Interfaces* **2021**, *8*, 2100206.
[6] S. Ohno, T. Bernges, J. Buchheim, M. Duchardt, A.-K. Hatz, M. A. Kraft, H. Kwak, A. L. Santhosha, Z. Liu, N. Minafra, F. Tsuji, A. Sakuda, R. Schlem, S. Xiong, Z. Zhang, P. Adelhelm, H. Chen, A. Hayashi, Y. S. Jung, B. V. Lotsch, B. Roling, N. M. Vargas-Barbosa, W. G. Zeier, *ACS Energy Lett.* **2020**, *5*, 910.
[7] K. Wagener, *Z. Phys. Chem.* **1960**, *23*, 305.
[8] H. Hoshino, M. Shimoji, *J. Phys. Chem. Solids* **1972**, *33*, 2303.
[9] H. Hoshino, H. Yanagiya, M. Shimoji, *J. Chem. Soc., Faraday Trans. 1* **1974**, *70*, 281.
[10] K. S. Kim, W.-K. Paik, *J. Chem. Eng. Data* **1975**, *20*, 356.
[11] H. Takamura, Y. Kuronuma, H. Maekawa, M. Matsuo, S. Orimo, *Solid State Ionics* **2011**, *192*, 118.
[12] T. Mezaki, Y. Kuronuma, I. Oikawa, A. Kamegawa, H. Takamura, *Inorg. Chem.* **2016**, *55*, 10484.
[13] Y. Inaguma, J. Yu, Y. Shan, M. Itoh, T. Nakamuraa, *J. Electrochem. Soc.* **1995**, *142*, L8.
[14] R. H. Radzilowski, J. T. Kummer, *J. Electrochem. Soc.* **1971**, *118*, 714.
[15] H. Wang, M. Yu, Y. Wang, Z. Feng, Y. Wang, X. Lü, J. Zhu, Y. Ren, C. Liang, *J. Power Sources* **2018**, *401*, 111.
[16] T. Famprikis, Ö. U. Kudu, J. A. Dawson, P. Canepa, F. Fauth, E. Suard, M. Zbiri, D. Dambournet, O. J. Borkiewicz, H. Bouyanfif, S. P. Emge, S. Cretu, J.-N. Chotard, C. P. Grey, W. G. Zeier, M. S. Islam, C. Masquelier, *J. Am. Chem. Soc.* **2020**, *142*, 18422.
[17] M. Kodama, S. Komiyama, A. Ohashi, N. Horikawa, K. Kawamura, S. Hirai, *J. Power Sources* **2020**, *462*, 228160.
[18] M. Kodama, A. Ohashi, S. Hirai, *J. Power Sources Adv.* **2020**, *4*, 100019.
[19] M. Nose, A. Kato, A. Sakuda, A. Hayashi, M. Tatsumisago, *J. Mater. Chem. A* **2015**, *3*, 22061.
[20] M. Cronau, M. Szabo, C. König, T. B. Wassermann, B. Roling, *ACS Energy Lett.* **2021**, *6*, 3072.
[21] S. W. Kurnick, *J. Chem. Phys.* **1952**, *20*, 218.
[22] B.-E. Mellander, D. Lazarus, *Phys. Rev. B* **1985**, *31*, 6801.
[23] C. A. Schneider, W. S. Rasband, K. W. Eliceiri, *Nat. Methods* **2012**, *9*, 671.
[24] D. Legland, I. Arganda-Carreras, P. Andrey, *Bioinformatics* **2016**, *32*, btw413.
[25] G. Landini, Novel context-based segmentation algorithms for intelligent microscopy, https://blog.bham.ac.uk/intellimic/g-landini-software/ (accessed April 2022).
[26] R. Heckel, *Trans. Metall. Soc. AIME* **1961**, *221*, 671.
[27] C. Sun, D. J. W. Grant, *Pharm. Dev. Technol.* **2001**, *6*, 193.
[28] C. M. Gabaude, M. Guillot, J. C. Gautier, P. Saudemon, D. Chulia, *J. Pharm. Sci.* **1999**, *88*, 725.
[29] R. C. Rowe, R. J. Roberts, in *Advances in Pharmaceutical Sciences* (Eds.: D. Ganderton, T. Jones, J. McGinity), Vol. *7*, Academic Press, Cambridge, MA **1995**, pp. 1–IV.
[30] J. A. Hersey, J. E. Rees, *Nat. Phys. Sci.* **1971**, *230*, 96.
[31] G. Vreeman, C. C. Sun, *Int. J. Pharm.: X* **2021**, *3*, 100094.
[32] J. Nordström, K. Welch, G. Frenning, G. Alderborn, *J. Pharm. Sci.* **2008**, *97*, 4807.
[33] K. S. Khomane, A. K. Bansal, *AAPS PharmSciTech* **2013**, *14*, 1169.
[34] S. Patel, A. M. Kaushal, A. K. Bansal, *Pharm. Res.* **2007**, *24*, 111.
[35] F. Mahmoodi, *Ph.D. Thesis*, Uppsala University **2012**.
[36] I. Ilić, B. Govedarica, R. Šibanc, R. Dreu, S. Srčič, *Int. J. Pharm.* **2013**, *446*, 6.
[37] P. Paronen, *Drug Dev. Ind. Pharm.* **1986**, *12*, 1903.
[38] S. Harm, A.-K. Hatz, I. Moudrakovski, R. Eger, A. Kuhn, C. Hoch, B. V. Lotsch, *Chem. Mater.* **2019**, *31*, 1280.
[39] T. Ates, A. Neumann, T. Danner, A. Latz, M. Zarrabeitia, D. Stepien, A. Varzi, S. Passerini, *Adv. Sci.* **2022**, *9*, 2105234.
[40] H. Chen, S. Adams, *IUCrJ* **2017**, *4*, 614.
[41] H. Chen, L. L. Wong, S. Adams, *Acta Cryst. B* **2019**, *75*, 18.
[42] L. L. Wong, K. C. Phuah, R. Dai, H. Chen, W. S. Chew, S. Adams, *Chem. Mater.* **2021**, *33*, 625.
[43] R. N. Jeffery, D. Lazarus, *J. Appl. Phys.* **1970**, *41*, 3186.
[44] P. C. Allen, D. Lazarus, *Phys. Rev. B* **1978**, *17*, 1913.
[45] D. N. Bose, G. Parthasarathy, D. Mazumdar, E. S. R. Gopal, *Phys. Rev. Lett.* **1984**, *53*, 1368.

[46] Y. Daiko, E. Takahashi, N. Hakiri, H. Muto, A. Matsuda, T. Rouxel, J.-C. Sangleboeuf, A. Mineshige, T. Yazawa, *Solid State Ionics* **2014**, *254*, 6.
[47] J. J. Fontanella, *J. Chem. Phys.* **1999**, *111*, 7103.
[48] Z.-H. Fu, X. Chen, C.-Z. Zhao, H. Yuan, R. Zhang, X. Shen, X.-X. Ma, Y. Lu, Q.-B. Liu, L.-Z. Fan, Q. Zhang, *Energy Fuels* **2021**, *35*, 10210.
[49] N. H. Nachtrieb, J. A. Weil, E. Catalano, A. W. Lawson, *J. Chem. Phys.* **1952**, *20*, 1189.
[50] H. Fei, M. Wiedenbeck, N. Sakamoto, H. Yurimoto, T. Yoshino, D. Yamazaki, T. Katsura, *Phys. Earth Planet. Inter.* **2018**, *275*, 1.
[51] BACI, A comprehensive multi-physics simulation framework, https://baci.pages.gitlab.lrz.de/website/ (accessed: October, 2022).
[52] A. Latz, J. Zausch, *J. Power Sources* **2011**, *196*, 3296.
[53] T. Danner, M. Singh, S. Hein, J. Kaiser, H. Hahn, A. Latz, *J. Power Sources* **2016**, *334*, 191.